



Contents lists available at ScienceDirect

International Journal of Rock Mechanics & Mining Sciences

journal homepage: www.elsevier.com/locate/ijrmms

A three invariant model of failure in true triaxial tests on Castlegate sandstone



J.W. Rudnicki

Department of Civil and Environmental Engineering, Northwestern University, 2145 Sheridan Road, Evanston, IL 60208-3109, USA

ARTICLE INFO

Keywords:

Sandstone
Failure
Three invariant
Intermediate principal stress
Lode angle

1. Introduction

By far the most common rock testing configuration is axisymmetric compression in which the most compressive principal stress (σ_1) is axial and the other two are equal and provide the lateral confinement. Somewhat less common is axisymmetric extension in which the least compressive stress (σ_3) is axial and the other two are again equal and provide the lateral confinement. Although these tests have provided an enormous amount of information about rock deformation and failure, they are limited in that the intermediate principal stress (σ_2) is always equal to the most or least compressive stress. Consequently, these tests are able to cover only a restricted range of possible stress states. Furthermore, axisymmetric stress states are not typical of those in the Earth's crust.^{1–4} Even when the tectonic stress field is nearly axisymmetric, the stress state around inhomogeneities, such as aquifers, reservoirs, mines or faults, will be fully three-dimensional.

In the 60's Mogi^{5,6} noted that the differences in failure stress between axisymmetric compression and extension tests indicated a dependence on the intermediate principal stress. As a result, he began to conduct true triaxial tests on cubical specimens in which all three principal stresses differed.^{6–8} Until recently, these tests were conducted primarily on low porosity rocks. Now, however, true triaxial tests have been done on higher porosity sandstones.^{9–15}

The conventional way in which true triaxial tests are done is that the specimen is first loaded in hydrostatic compression, then stresses are increased on two of the faces until the desired level of the intermediate principal stress, σ_2 , is reached, and finally the stress on one of the faces is increased to failure.^{5,6,13,16} Consequently, two of the three principal stresses are constant. Although this loading suffices to study the role of σ_2 on failure, it has disadvantages for understanding

the physical processes of failure. In particular, both the hydrostatic (mean normal) stress and the deviatoric stress state (defined more precisely below) change during loading to failure. An exception to this conventional loading is plane strain loading.^{12,17–19} Because the intermediate stress is controlled to maintain approximately plane strain conditions, it is changing during loading to failure. Consequently, both the hydrostatic stress and the deviatoric stress state are also changing for this loading.

Recent true triaxial tests have been conducted in which the deviatoric stress state is held constant. In tests on two porous sandstones, Coconino and Bentheim, Ma et al.^{11,14} maintain σ_3 constant and raise the two other principal stresses in a fixed ratio to keep the deviatoric stress state constant. The hydrostatic stress is not, however, constant. Ingraham et al.^{9,10} have conducted unique tests on Castlegate sandstone in which they control changes in all three principal stresses in order to keep both the deviatoric stress state and the hydrostatic stress constant. Then the magnitude of the deviatoric stress is increased to failure.

In this note, a simple failure condition introduced by Rudnicki²⁰ is applied to the data of Ingraham et al.¹⁰ on Castlegate sandstone. Application of this condition provides additional interpretation of the results and a means of generalizing them to arbitrary stress states.

2. Preliminaries

Denote the principal stresses (positive in compression) by $\sigma_1 \geq \sigma_2 \geq \sigma_3$. The mean normal stress is

$$\sigma = \frac{1}{3}(\sigma_1 + \sigma_2 + \sigma_3) \quad (1)$$

E-mail address: jwru@northwestern.edu.

<http://dx.doi.org/10.1016/j.ijrmms.2017.06.007>

Received 15 February 2017; Received in revised form 12 June 2017; Accepted 22 June 2017
1365-1609/ © 2017 Elsevier Ltd. All rights reserved.

If the principal stresses are plotted along axes, then the hydrostat ($\sigma_1 = \sigma_2 = \sigma_3$) is the line that makes equal angles with the axes. Because the mean normal stress is constant in planes perpendicular to this line (the so-called octahedral or Π planes), the stress states in these planes are purely deviatoric. Hence, points in these planes are located by principal values of the deviatoric stress, with components given by

$$s_{ij} = \sigma_{ij} - \frac{1}{3}\delta_{ij}\sigma_{kk} \tag{2}$$

The Mises equivalent stress (equal to $\sqrt{3/2}$ the octahedral shear stress) is

$$\tau = \sqrt{\frac{1}{2}s_{ij}s_{ij}} \tag{3}$$

The repeated subscript denotes summation and δ_{ij} is the Kronecker delta ($=1$, if $i = j$, $=0$, otherwise). The Mises equivalent stress can be written in terms of the principal stresses as

$$\tau = \sqrt{\frac{1}{6}\{(\sigma_1 - \sigma_2)^2 + (\sigma_2 - \sigma_3)^2 + (\sigma_3 - \sigma_1)^2\}} \tag{4}$$

and this expression makes it clear that τ depends only on differences in the principal stresses. Radial distance in deviatoric planes is given by τ and angular position can be described by a Lode angle Θ . This angle can be defined in different ways but here it is²¹

$$\sin 3\Theta = -\frac{\sqrt{27}J_3}{2\tau^3} \tag{5}$$

where J_3 is the third invariant of the deviatoric stress,

$$J_3 = (1/3)s_{ij}s_{jk}s_{ki} = (1/3)(s_1^3 + s_2^3 + s_3^3) \tag{6}$$

and the second equality applies for the principal deviatoric stresses. An alternative expression for the Lode angle is²²

$$\tan \Theta = \frac{\sigma_1 + \sigma_3 - 2\sigma_2}{\sqrt{3}(\sigma_1 - \sigma_3)} \tag{7}$$

Because the Lode angle depends only on the ratios of the principal deviatoric stresses it specifies the deviatoric stress state. The particular definition of Lode angle, (5) and (7), is zero for a stress state of deviatoric pure shear $\sigma_2 = (\sigma_1 + \sigma_3)/2$, corresponding to $s_2 = \sigma_2 - \sigma = 0$ where s_2 is the intermediate principal deviatoric stress. For axisymmetric compression ($\sigma_1 > \sigma_2 = \sigma_3$) $\Theta = 30^\circ$ and for axisymmetric extension ($\sigma_3 < \sigma_1 = \sigma_2$) $\Theta = -30^\circ$.

Fig. 1 shows the geometry in deviatoric planes. Because the normal components of the deviatoric stress must sum to zero, the axes are at 120° in these planes. The sector $-30^\circ \leq \Theta \leq 30^\circ$ corresponds to $\sigma_1 \geq \sigma_2 \geq \sigma_3$. If the material is isotropic, and Castlegate sandstone is

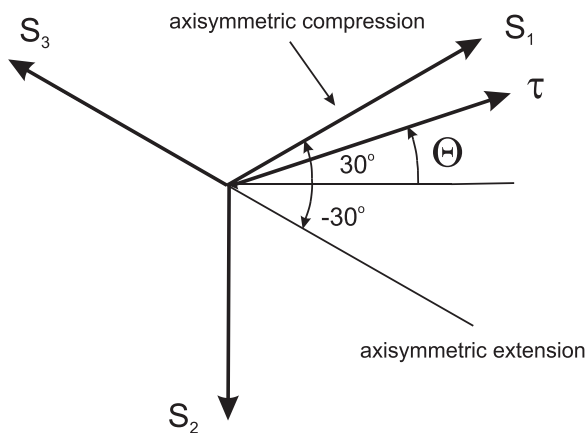


Fig. 1. Geometry in deviatoric planes. s_1 , s_2 and s_3 are principal values of the deviatoric stress and the axes are 120° apart. These axes are the projections of the axes on which the principal stresses are plotted. The sector $-30^\circ \leq \Theta \leq 30^\circ$ corresponds to $\sigma_1 \geq \sigma_2 \geq \sigma_3$ and for an isotropic material all deviatoric stress states are defined by position in this sector.

approximately so,¹⁰ the ordering of the stresses is immaterial. Consequently, for an isotropic material, the remaining five sectors correspond to reordering the principal stresses and can be obtained by symmetry and reflection. Thus, it suffices to consider only this 60° sector.

3. Failure condition

Rudnicki²⁰ suggested a three invariant yield condition that is used here as failure condition. The condition takes the following simple form in terms of the Lode angle Θ and the Mises equivalent stress τ :

$$F(\tau, \sigma, \Theta) = -\sqrt{\frac{4}{27}}A(\sigma)\sin(3\Theta)\left(\frac{\tau}{\tau_0(\sigma)}\right)^3 + \left(\frac{\tau}{\tau_0(\sigma)}\right)^2 - 1 = 0 \tag{8}$$

where $-1 \leq A \leq 1$. $A(\sigma)$ and $\tau_0(\sigma)$ are calibration functions. For $-1 \leq A \leq 1$ the roots of (8) are all real and the relevant root is the one nearest to one. An analytic solution for the roots can be given, but in practice it is more convenient to solve for them numerically. For deviatoric pure shear, $\Theta = 0^\circ$, the first term is absent and failure occurs at $\tau = \tau_0(\sigma)$. Thus, failure in deviatoric pure shear determines the calibration function $\tau_0(\sigma)$.

As explained by Rudnicki,²⁰ (8) is a generalized form of conditions introduced by Lade and Duncan²³ and Matsuoka and Nakai²⁴ (also see Borja et al.²⁵) and reduces to them for particular constant values of A and linear $\tau_0(\sigma)$. An advantage of the form (8) is that the dependence of τ_0 and A on σ can be chosen to agree with particular data sets.

Fig. 2 plots (8) in the deviatoric plane for several values of A : 0.0, 0.5, 0.7 and 0.9. As already mentioned, the principal stresses can be reordered for an isotropic material and, consequently, the shape of the surface is determined by the sector $-30^\circ \leq \Theta \leq 30^\circ$. The remaining five sectors are obtained by reflection and symmetry. For $A = 0$, (8) reduces to a (possibly nonlinear) Drucker-Prager condition²⁶ and the shape is circular. As A increases the shape becomes a rounded triangle as are the Lade and Duncan²³ and Matsuoka and Nakai²⁴ criteria. For $A = 1$, the shape is triangular, as for a Rankine material in which failure occurs at a critical value of the smallest (least compressive) principal stress. For $A < 0$, the shapes are the same, but are reflected about the horizontal axis.

The value of A controls the difference between $\tau/\tau_0(\sigma)$ at failure in axisymmetric extension and axisymmetric compression. For $A > 0$, the value of τ/τ_0 for axisymmetric compression exceeds that for axisymmetric extension and the reverse is true for $A < 0$. Fig. 3 plots the ratio

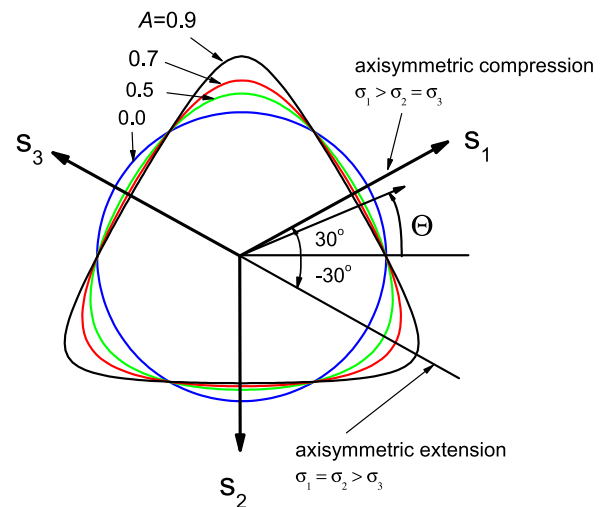


Fig. 2. Failure surfaces in deviatoric planes are shown for four values of A : 0.0, 0.5, 0.7, 0.9. For $A < 0$, the shapes are the same, but are reflected about the horizontal axis. The shape of the surface is determined by the sector $-30^\circ \leq \Theta \leq 30^\circ$ and the remaining five sectors are obtained by reflection and symmetry.

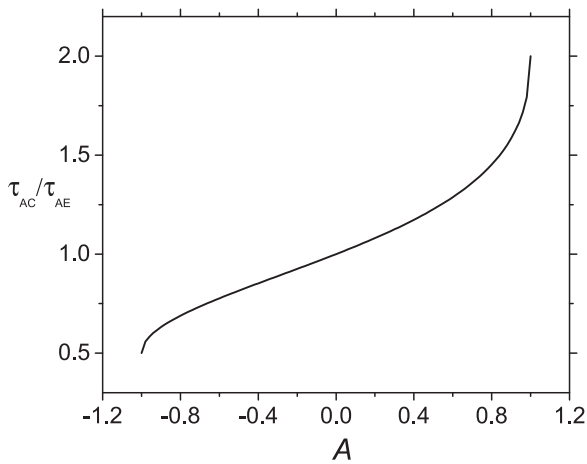


Fig. 3. Ratio of the shear stress at failure in axisymmetric compression to axisymmetric extension as a function of the parameter A . The ratio equals $\sqrt{3}/2$ for $A = -1$ and 2 for $A = +1$.

of τ at failure in axisymmetric compression to that in axisymmetric extension as a function of A . As shown the ratio varies from $\sqrt{3}/2$ for $A = -1$ to 2 for $A = +1$.

Haimson and Rudnicki²⁷ have used (8) as a yield condition to infer material properties from observed failure angles for two siltstones and Ma et al.¹⁵ have used the same procedure for two porous sandstones, Coconino and Bentheim. Ma et al.^{11,14} have used it as a failure condition for the same two sandstones. Here we apply (8) to the true triaxial data of Ingraham et al.¹⁰ on Castlegate sandstone.

4. Application to Castlegate sandstone data

Ingraham et al.¹⁰ have conducted the first true triaxial tests in which both the mean stress σ and the Lode angle θ are kept constant while τ is increased to failure. Consequently, it is possible to trace out the failure surface in planes of constant mean stress. Tests were conducted at five mean stresses, 30 MPa, 60 MPa, 90 MPa, 120 MPa, and 150 MPa and five Lode angles 30° (axisymmetric compression, ASC), 14.5° (ASCPS), 0° (deviatoric pure shear, PS), -14.5° (ASEPS), and -30° (axisymmetric extension, ASE).

Fig. 4 shows the data of Ingraham et al.¹⁰ from their Fig. 13 in which they plot τ vs. σ for the five Lode angles. Note that at the highest mean stress the value of τ at failure has begun to decrease with σ indicating the emergence of a cap, as also noted in Ingraham et al.¹⁰ The data for $\theta = 0$ is well described by the quadratic function

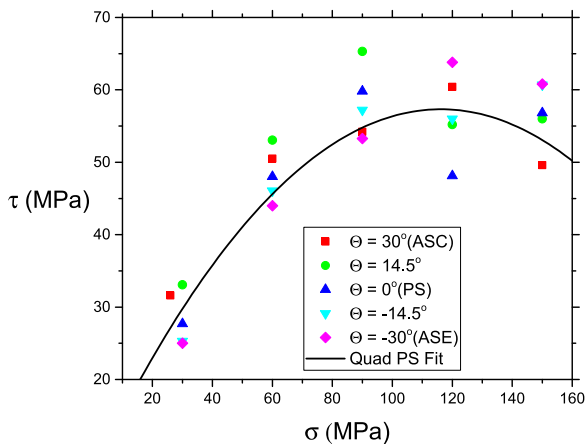


Fig. 4. Shear stress at failure τ versus mean stress σ from the data of Ingraham et al.¹⁰ for five values of mean stress and five values of Lode angle. Curve is a quadratic fit through the data for deviatoric pure shear $\theta = 0^\circ$ and determines the function $\tau_0(\sigma)$.

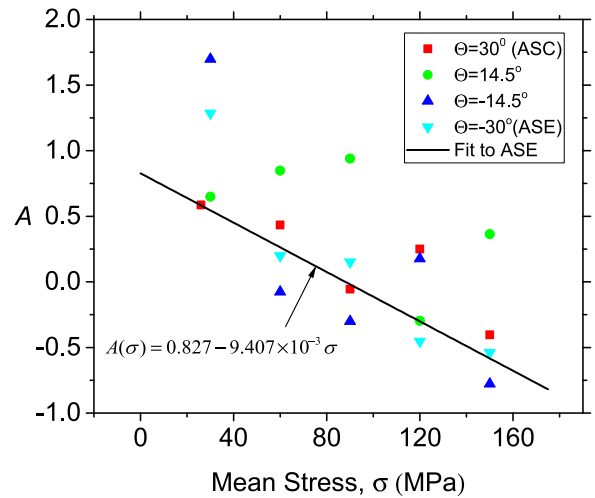


Fig. 5. Calculated values of A for the function $\tau_0(\sigma)$ for the Lode angles other than 0° . Line is fit to the values for axisymmetric extension ($\theta = -30^\circ$).

$$\tau_0(\sigma) = 7.216 + 0.826\sigma - (3.711 \times 10^{-3})\sigma^2 \quad (9)$$

where σ is in MPa. This determines $\tau_0(\sigma)$.

Now (8) is solved for

$$A(\sigma) = \frac{(\tau/\tau_0(\sigma))^2 - 1}{\sqrt{4/27} (\tau/\tau_0(\sigma))^3 \sin(3\theta)} \quad (10)$$

Fig. 5 plots the points obtained by substituting the measured values of τ and σ for Lode angles other than $\theta = 0^\circ$. In this plot the data exhibit considerable scatter. In particular, the values of A for $\theta = -14.5^\circ$ and $\theta = -30^\circ$ (axisymmetric extension) at the lowest mean stress, 30 MPa, are greater than one and, thus, lie outside the allowable range of A ($-1 \leq A \leq +1$). This may occur because of experimental variability or because the form (8) is not sufficiently flexible at the lowest mean stresses. In addition, the points for $\theta = 14.5^\circ$ do not seem to follow the trend of the other data. Given the scatter, a straight line is fit to the data for axisymmetric extension omitting the point for $\sigma = 30$ MPa:

$$A(\sigma) = 0.827 - 9.407 \times 10^{-3} \sigma \quad (11)$$

where, again, σ is in MPa. Fitting a line to the points for axisymmetric compression might seem a better choice since all five points fall within the allowable range of A . But, as explained by Ingraham et al.¹⁰, the boundary conditions in the testing apparatus for axisymmetric compression are a little different. In fact, fitting a line to axisymmetric compression makes little difference.

Once the functions $\tau_0(\sigma)$ and $A(\sigma)$ have been determined, the variation of $\tau(\sigma)$ with σ can be calculated for Lode angles other than $\theta = 0^\circ$. These are shown in Fig. 6. The calculated curves are compared with data from Fig. 4 and a quadratic fit to the data. The agreements between the calculated variation and the quadratic fits are good except for the Lode angle $\theta = 14.5^\circ$.

Fig. 7 reconstructs the data from Fig. 14b of Ingraham et al.¹⁰ showing the shape of the failure surface in planes of constant mean stress. As in the plot of Ingraham et al.¹⁰ the point for axisymmetric compression is omitted because, as already mentioned, the boundary conditions for the testing apparatus are slightly different for this loading. In order to more easily visualize the shape of the failure surface, symmetry and reflection (assuming isotropy) have been used to extend the data from the sector $-30^\circ \leq \theta \leq 30^\circ$ to the complete range of angles. Fig. 7 also shows the failure surfaces determined from (8) with the values of $\tau_0(\sigma)$ and $A(\sigma)$ determined from the data. Despite the qualification about the different values of A for different Lode angles in Fig. 5, the agreement is reasonable. For the lowest mean stress tested the failure surface is a rounded triangular surface pointed downward (toward positive s_2). As the mean stress increases the

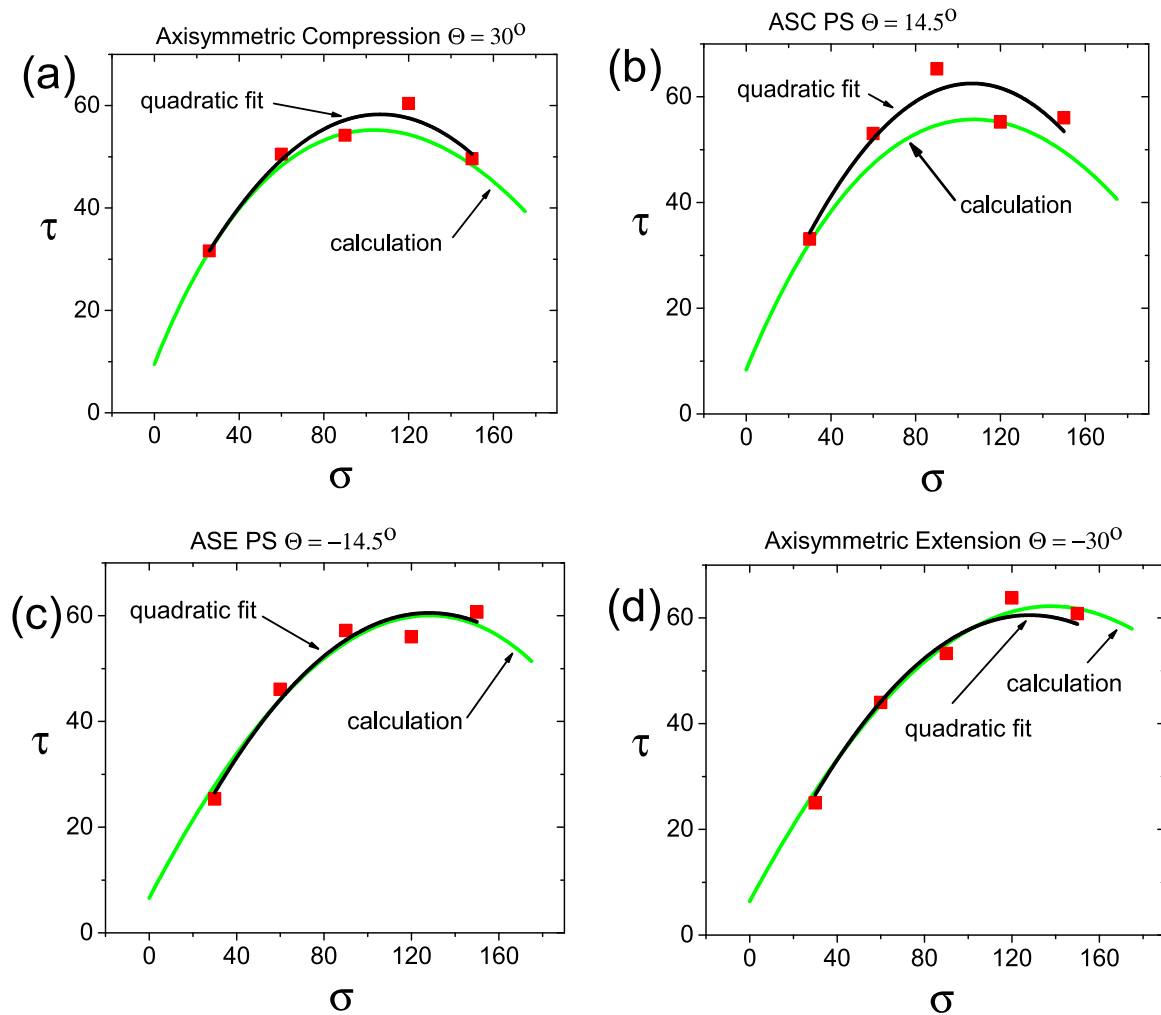


Fig. 6. Calculated variation of shear stress τ (MPa) at failure versus mean stress σ (MPa) for Lode angles other than $\theta = 0^\circ$ using the empirically fitted functions $\tau_0(\sigma)$ and $A(\sigma)$. Also shown are the data from Fig. 4 and quadratic fits to the data.

surface becomes more circular. At the highest mean stress, it evolves to a rounded triangle but with the point upward (toward negative s_2). This inversion of the triangular shape is caused by the change in sign in A from positive to negative as the mean stress increases (Fig. 5).

5. Discussion

Ma et al.^{11,14} have used (8) to model failure of Coconino and Bentheim sandstones. As with the Castlegate $\tau_0(\sigma)$ is well described by a quadratic function. For Coconino, $\tau_0(\sigma)$ increases with σ for the range tested. For the Bentheim $\tau_0(\sigma)$ first increases with σ but then begins to decrease at the higher values as it does for the Castlegate (see Figs. 4 and 6). The appearance of a descending portion of the $\tau_0(\sigma)$ vs. σ curve indicates the incipient formation of a cap and is apparently due to the higher porosities of the Bentheim (24%) and the Castlegate (26%) compared with Coconino (17.5%). This descending portion is associated with the appearance of compaction bands in the Castlegate and Bentheim. Similar to Fig. 6, the inferred values of A for the Coconino and Bentheim are scattered, but are fit adequately by a straight line except for the Bentheim at low mean stress (less than about 50 MPa).

When the inferred values of $A(\sigma)$ and $\tau_0(\sigma)$ are used to predict $\tau_0(\sigma)$ vs. σ curves for Lode angles other than $\theta = 0$ (Fig. 3 of Ma et al.¹⁴) the agreement is good except for axisymmetric compression. For axisymmetric compression of the Bentheim at low mean stress the prediction is particularly poor because of the inadequacy of a linear approximation to $A(\sigma)$ in this region. The agreement with the data is also good

when the prediction is used to plot σ_1 at failure against σ_3 (their Fig. 10). (The R^2 value given for the Bentheim in axisymmetric extension is a misprint; it should be 0.97, not 0.17.)

Because the mean stress varies during their tests Ma et al.¹⁴ are not able to plot their data directly in deviatoric planes as in Fig. 7 here. They do so, however, by interpolating the data for τ at different mean stresses. The results, shown in their Figs. 4 and 5, are similar to those here. At low mean stresses, the failure surface is a rounded triangle with the point down. For the Coconino, the failure surface becomes more rounded with higher mean stress and is nearly circular for the highest mean stress. The Bentheim failure surface becomes more circular as the mean stress increases but is a rounded triangle with the point up at the highest mean stress. As with the Castlegate, the emergence of the inverted rounded triangle at the highest mean stress is related to the descending portion of the $\tau_0(\sigma)$ curve. The agreement between data and predictions is good. An exception is the Bentheim at $\sigma = 300$ MPa (their Fig. 5f) because the largest mean stress achieved in the experiments is only about 250 MPa for Lode angles between deviatoric pure shear and axisymmetric compression.

The fit between data and predictions here for the Castlegate is reasonably good. The predicted curves of $\tau_0(\sigma)$ vs. σ agree well with the curves fit to the data in Fig. 6, except for $\theta = 14.5^\circ$ (which, as noted earlier, does not follow the trend of the other data). Although the predictions agree reasonably well with data in Fig. 7, there are discrepancies. Some of this may be due to experimental variability, but limitations of the form of (8) are a factor. A depends only on σ in

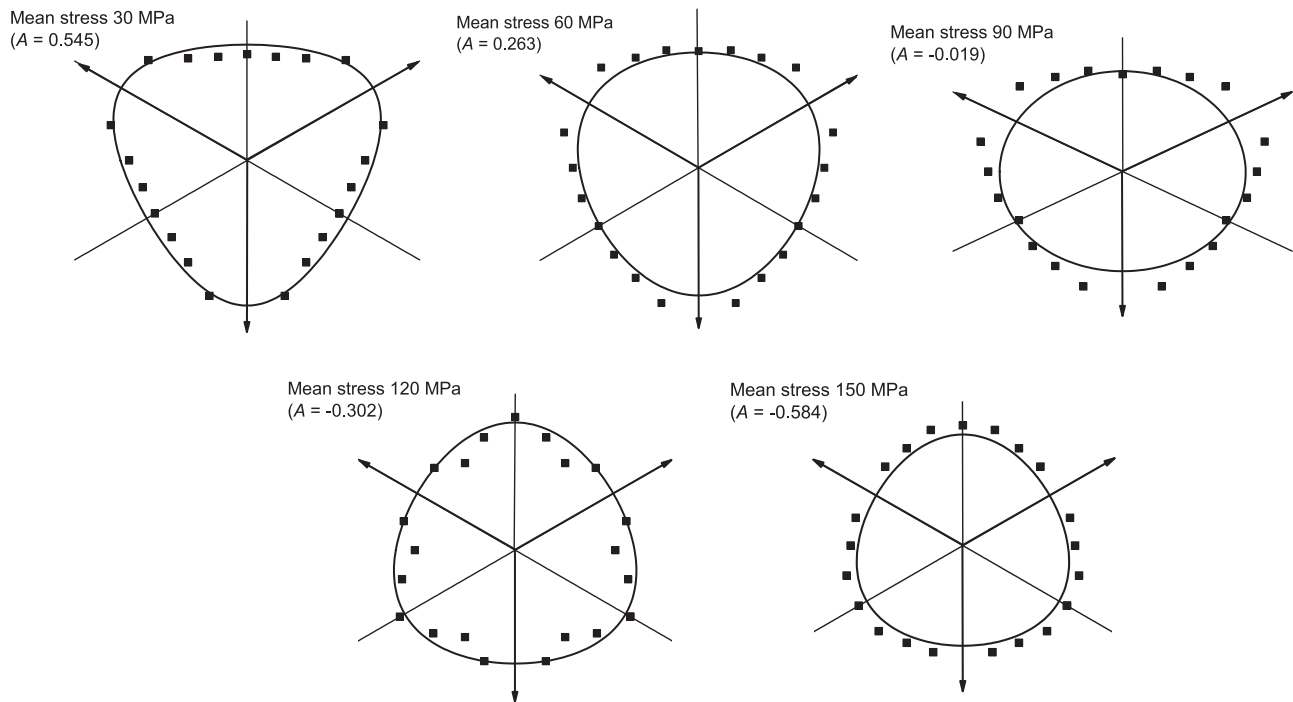


Fig. 7. Points are data of Ingraham et al.¹⁰ for τ at failure (peak stress) for different fixed values of mean stress σ and different Lode angles Θ . Points for axisymmetric compression ($\Theta = 30^\circ$) are omitted. Solid curves are the calculated values of (8) with the fitted values of $\tau_0(\sigma)$ from Fig. 4 and $A(\sigma)$ from Fig. 5. For the purpose of visualization points and curves are extended by symmetry and reflection to the full range of Lode angles from the sector $-30^\circ \leq \Theta \leq 30^\circ$.

(8). Even allowing for experimental variability and discounting the data for $\Theta = 14.5^\circ$, Fig. 5 suggests a dependence of A on the Lode angle. This implies that the form of (8) is not sufficient to capture fully the dependence of the data on Θ . In principle, dependence of A on Θ could be incorporated but this would undermine the simplicity and generality of the model. An alternative approach would be reformulation of the failure condition. How to do this in a way that maintains the desirable features of isotropy and convexity is not clear and could be the subject of future work. In spite of its limitations, the more flexible form of (8) has advantages over the Matsuoka-Nakai²⁴ and Lade-Duncan²³ conditions that are widely used.

6. Conclusion

This note has presented a simple failure condition, introduced as a yield condition by Rudnicki,²⁰ that generalizes conditions of Lade and Duncan²³ and Matsuoka and Nakai.²⁴ The condition is easily calibrated by the data of Ingraham et al.¹⁰ It allows for arbitrary dependence of the shear stress at failure on the mean stress and on changes of shape in the deviatoric plane with mean stress. The calibrated condition describes the Castlegate data of Ingraham et al.¹⁰ reasonably well. The calculations indicate a change in the shape of the failure surface with increasing mean stress from a rounded triangle with the point up to more circular and then to a rounded triangle with the point down. The condition can be used to extend the data to arbitrary stress states for use in numerical calculations.

Acknowledgement

I am grateful to Mathew Ingraham for providing the data and to Xiaodong Ma and Bezalel Haimson for helpful comments on the manuscript. The comments of an associate editor and a reviewer improved the manuscript. This research did not receive any specific grant from funding agencies in the public, commercial, or not-for-profit sectors.

References

- Haimson B. The hydrofracturing stress measuring method and recent field results. *Int J Rock Mech Min Sci.* 1978;15:167–178.
- McGarr A, Gay NC. State of stress in the Earth's crust. *Annu Rev Earth Planet Sci.* 1978;6:405–436.
- Brace WR, Kohlstedt DL. Limits on lithospheric stress imposed by laboratory experiments. *J Geophys Res.* 1980;85(B11):6248–6252.
- Vernik L, Zoback M. Estimation of maximum horizontal principal stress magnitude from stress-induced well bore breakouts in the Cajon Pass Scientific Research Borehole. *J Geophys Res.* 1992;97(B4):5109–5119.
- Mogi K. Effect of the intermediate principal stress on rock failure. *J Geophys Res.* 1967;72:5117–5131.
- Mogi K. Experimental rock mechanics. *Volume 3 of Geomechanics Research Series.* Taylor and Francis; 2007, ISBN 0-415-39443-0.
- Mogi K. Effect of the triaxial stress system on the failure of dolomite and limestone. *Tectonophysics.* 1971;11:111–127.
- Mogi K. Fracture and flow of rocks. *Tectonophysics.* 1972;13(1-4):541–568 [In: Ritsema AR, ed. *The Upper Mantle.*]
- Ingraham MD, Issen KA, Holcomb DJ. True triaxial testing of Castlegate sandstone. In: *Proceedings of 44th U.S. Rock Mechanics Symposium and 5th U.S. Canada Rock Mechanics Symposium.* Salt Lake City, UT, June 27–30 2010. American Rock Mechanics Association; 2010.
- Ingraham MD, Issen KA, Holcomb DJ. Response of Castlegate sandstone to true triaxial states of stress. *J Geophys Res.* 2013;118:536–552. <http://dx.doi.org/10.1002/jgrb.50084>.
- Ma X, Rudnicki JW, Haimson B. True triaxial tests in two porous sandstones: experimental failure characteristics and theoretical prediction. In: *Proceedings of the 48th US Rock Mechanics/Geomechanics Symposium.* Minneapolis, MN, USA, 1–4 June 2014, number 14-7286. American Rock Mechanics Association; 2014.
- Makhnenko RY, Harvieux J, Labuz JF. Paul-Mohr-Coulomb failure surface of rock in the brittle regime. *Geophys Res Lett.* 2015;42:6975–6981. <http://dx.doi.org/10.1002/2015GL065457>.
- Ma X, Haimson B. Failure characteristics of two porous sandstones subjected to true triaxial stresses. *J Geophys Res Solid Earth.* 2016;121:6477–6498. <http://dx.doi.org/10.1002/2016JB012979>.
- Ma Xiaodong, Rudnicki John W, Haimson Bezalel C. The application of a modified Lade-Duncan-Matsuoka-Nakai failure criterion to two porous sandstones. *Int J Rock Mech Min Sci.* 2017;92:9–18. <http://dx.doi.org/10.1016/j.ijrmmms.2016.12.004>.
- Ma X, Rudnicki JW, Haimson BC. Failure characteristics of two porous sandstones subjected to true triaxial stresses: applied through a novel loading path. *J Geophys Res Solid Earth.* 2017.
- Haimson Bezalel. True triaxial stresses and the brittle fracture of rock. *Pure Appl Geophys.* 2006;163:1101–1130. <http://dx.doi.org/10.007/s00024-006-0065-7>.
- Holcomb DJ, Rudnicki JW. Inelastic constitutive properties and shear localization in Tennessee marble. *Int J Numer Anal Methods Geomech.* 2001;25:109–129.

- 18 Makhnenko RY, Labuz JF. Plane strain testing with passive restraint. *Rock Mech Rock Eng.* 2014;47:2021–2029. <http://dx.doi.org/10.1007/s00603-013-0508-2>.
- 19 Labuz JF, Makhnenko RY, Harvieux JT. Failure criterion with intermediate stress and two friction angles. In: *Proceedings of the 50th U.S. Rock Mechanics/ Geomechanics Symposium*. Houston, Texas, USA, 26–29 June 2016, number 16-620. American Rock Mechanics Association; 2016.
- 20 Rudnicki John W. Failure of rocks in the laboratory and in the Earth. In: James P. Denier, Matthew D. Fine, editors, *Mechanics Down Under, Proceedings of the 22nd International Congress on Theoretical and Applied Mechanics* (pp. 199–215), Adelaide, Australia, 24–29 August 2008. Springer; 2013. <http://dx.doi.org/10.1007/978-94-007-5968-8>.
- 21 Borja Ronaldo I. *Plasticity Modeling and Computation*, Berlin: Springer; 2013. <http://dx.doi.org/10.1007/978-3-642-38547-6> [ISBN 978-3-642-38546-9].
- 22 Hill R. *The Mathematical Theory of Plasticity*. Oxford Engineering Science Series, London: Oxford; 1950.
- 23 Lade PV, Duncan JM. Elastoplastic stress-strain theory for cohesionless soil. *J Geotech Eng Div ASCE.* 1975;101:1037–1053.
- 24 Matsuoka H, Nakai T. Stress-deformation and strength characteristics of soil under three different principal stresses. In: *Proceedings of the Japan Soc. Civil Eng.* (pp. 1037–1053); 1974.
- 25 Borja Ronaldo I, Sama Kossi M, Sanz Pablo F. On the numerical integration of three-invariant elastoplastic constitutive models. *Comput Methods Appl Mech Eng.* 2003;192:1227–1258. [http://dx.doi.org/10.1016/S0045-7825\(02\)00620-5](http://dx.doi.org/10.1016/S0045-7825(02)00620-5).
- 26 Drucker DC, Prager W. Soil mechanics and plastic analysis for limit design. *Q J Appl Math.* 1952;10(2):157–165.
- 27 Haimson Bezael, Rudnicki John W. The effect of the intermediate principal stress on fault formation and fault angle in siltstone. *J Struct Geol.* 2010;32:1701–1711.